

Surface Waves on a Semi-toroidal Water Ring

Sunghwan Jung ¹, Erica Kim ¹, Michael J. Shelley ¹, and Jun Zhang ^{2,1}

¹ *Applied Mathematics Laboratory, Courant Institute of Mathematical Sciences, New York University, 251 Mercer Street, New York, New York 10012, USA*

² *Department of Physics, New York University, 4 Washington Place, New York, New York 10003, USA*

(Dated: February 9, 2020)

We study the dynamics of surface waves on a semi-toroidal ring of water that is excited by vertical vibration. We create this specific fluid volume by patterning a glass plate with a hydrophobic coating, which confines the fluid to a precise geometric region. To excite the system, the supporting plate is vibrated up and down, thus accelerating and decelerating the fluid ring along its toroidal axis. When the driving acceleration is sufficiently high, the surface develops a standing wave, and at yet larger accelerations, a travelling wave emerges. These different surface waves also depend on driving frequency.

PACS numbers: 47.54.-r, 47.20.Ma, 47.35.-i

In 1831, Faraday first observed that surface waves on a vibrated fluid volume oscillate at half the driving frequency [1]. These *Faraday waves* demonstrate the surface instability caused by strong oscillatory accelerations exerted on the fluid volume. Benjamin & Ursell showed that the amplitude of a surface eigenmode obeys the Mathieu equation [2, 3]. It follows that the superposition of multiples of harmonics and subharmonics are also solutions to the Mathieu equation. In the presence of finite viscosity, however, the subharmonic response is dominant [4, 5, 6].

Recent experiments have revealed that patterns of various symmetries, such as striped [7, 8], triangular [9], square [10, 11, 12], and hexagonal [13, 14], can be excited on the free surface of a fluid layer. Quasi-one dimensional surface waves have also been studied in both narrow annular and channel geometries [15, 16, 17, 18]. In these experiments, the standing waves often interact with the meniscus that forms at the bounding walls. The contact point and length-scale of this meniscus continually change as a result of the vertical oscillations. Consequently, the meniscus emits waves towards the bulk [16]. In other experiments, to remove this meniscus effect, the contact point is pinned on a sharp edge or brim [19, 20, 21].

A curved fluid surface, such as on a hemi-spherical drop [22, 23, 24], has been used to study surface waves in a confined geometry without bounding walls. Vibrating the drop causes waves to form on the curved surface, and for high external forcing, droplets are ejected. This process, termed *atomization*, provides one way to create a spray [25, 26]. The instability of the drop's semi-spherical surface has been utilized for spray cooling, mixing, and humidification.

Other curved geometries have been less studied, perhaps due to difficulties in creating more complex bounding geometries for a droplet. Here, we employ a hydrophobic/hydrophilic patterning of a surface to confine a water volume to a specific region. In particular,

if part of a hydrophilic substrate (low surface energy) is covered by a hydrophobic coating (high surface energy; we use Fluorothane ME; Cytonix Corp.), water is prevented from spreading beyond the hydrophilic region. The boundary between the two regions acts as an edge upon which the fluid contact point is pinned.

In the experiment we report here, the hydrophilic region is a thin annulus, and water placed there forms into a semi-toroidal volume with two pinned contact lines. We find that surface waves first develop along the centerline of the torus, which allows us to study quasi-one dimensional waves on a curved surface.

The schematic of our experimental setup is shown in Fig. 1. The annular hydrophilic region has inner radius $a_1 = 2.5$ cm and outer radius $a_2 = 3.5$ cm. The patterned glass plate is rigidly connected to a speaker, which oscillates the plate vertically at a controlled driving frequency and amplitude. A high-speed video camera is centered above the plate along the axis of the annulus. Since the semi-torus of water has a cross-sectional radius ($r \approx 0.5$ cm) that is relatively small in comparison to the distance between the plate and the camera, bright regions of the water ring seen in top-viewed video frames correspond to local extrema of the fluid surface height.

We use a systematic procedure to define the onset of surface waves. At fixed driving frequencies $\Omega/2\pi$ between 20 Hz and 65 Hz, the amplitude of oscillation is slowly increased until the fluid surface loses stability to azimuthally modulated standing waves. For each driving frequency, a distinct wave pattern is observed. Figures 2a and b show these standing waves for two different driving frequencies. At 22 Hz (a), the wave pattern has 12 nodes (that is, 12 crossings of the wave peak along the annular mid-line). The left half of Fig. 2(a) shows a snapshot of the surface wave, whereas the right half is the image of two superimposed surface waves in different phases. In the snapshot, the cross-sectional shapes, or onset modes, of the fluid surface are shown as insets when cutting across the **I** and **II** lines. The overlapped image

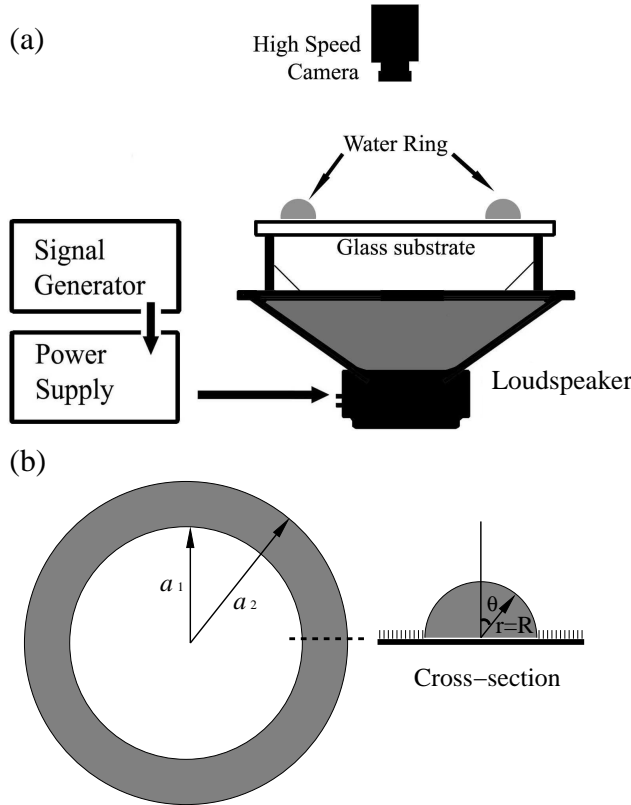


FIG. 1: (a) Side-view of the experimental set-up: a semi-toroidal water-ring on the hydrophobic patterned glass plate that is vibrated vertically by a loudspeaker. (b) Top and cross-sectional views of the water-ring.

demonstrates that standing waves are formed at half the driving frequency (22 Hz) near the onset. Increasing the driving frequency to 36 Hz increases the number of wave nodes to 24 (see Fig. 2b). Near the onset, as the driving frequency increases, the number of nodes increases monotonically (and discretely, due to the geometry), as is shown in Fig. 3.

To describe the instability of the azimuthally modulated surface waves seen in Fig. 2, we use an approximate inviscid model by considering coupled modes of surface waves. Rather than using the exact semi-toroidal geometry for our calculations, we neglect the annular curvature and use a cylindrical geometry instead. The variable r is the radius of the cross-section in cylindrical coordinate (see Fig. 1b). A water surface without external vibration is given by $r = r_0(\theta)$, where the dependence of r on θ is due to balancing gravity and surface tension. While the capillary length ($\sqrt{2\sigma/\rho g}$) of water is 0.4 cm, which is of the same order of cylinder radius $R = 0.5$ cm, we assume for simplicity that the unperturbed surface profile is close to a semi-circle with constant radius R . Small fluctuations of the surface can then be expressed as $R + \zeta$, where ζ is a small radial displacement deviating from R .

A linear form of Bernoulli equation with a velocity po-

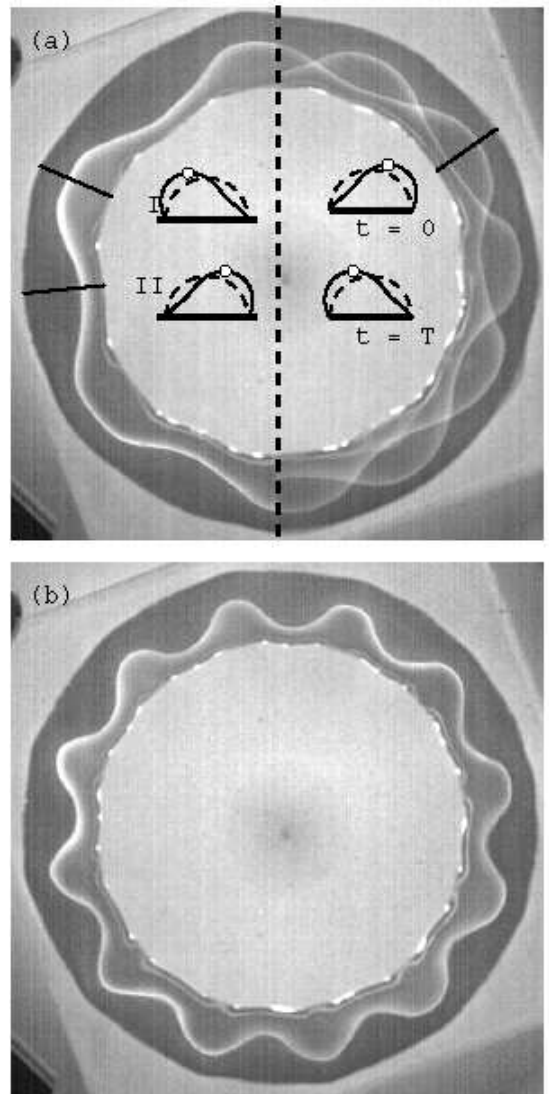


FIG. 2: Images of surface waves emerging from the water ring. At the driving frequency 22 Hz, 12 nodes are excited in the azimuthal direction (a), whereas 24 nodes appear at 36 Hz (b). In (a), the cross-sectional shapes along lines I (referred to as the peak) and II (trough) are shown schematically. The dashed curves represent the fluid surfaces in equilibrium. White dots represent the cross-section position of the bright curve in a top-viewed image. The right half of image (a) is an overlap of two photographs differing by the period of excitation T ($=1/22$ sec).

tential ϕ [2] is

$$g_e \zeta \cos \theta + \frac{\partial \phi}{\partial t} - \frac{\sigma}{\rho} \left(\frac{\zeta}{R^2} + \frac{1}{R^2} \frac{\partial^2 \zeta}{\partial \theta^2} + \frac{\partial^2 \zeta}{\partial z^2} \right) = 0, \quad (1)$$

$$\nabla^2 \phi = 0, \quad (2)$$

where $g_e(t) = g + a \cos t$ is the oscillating body force and σ is surface tension. By using $v_r|_{r=R} \equiv \partial_r \phi|_{r=R} = \partial_t \zeta$ which neglects the nonlinear terms in the kinematic

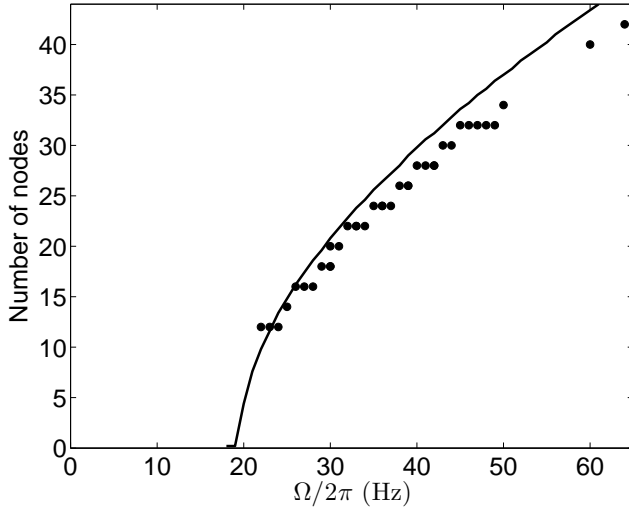


FIG. 3: Number of nodes around the annulus observed near the onset of wave formation. Dots are from experiments. The solid line is a result of the inviscid coupled linear model.

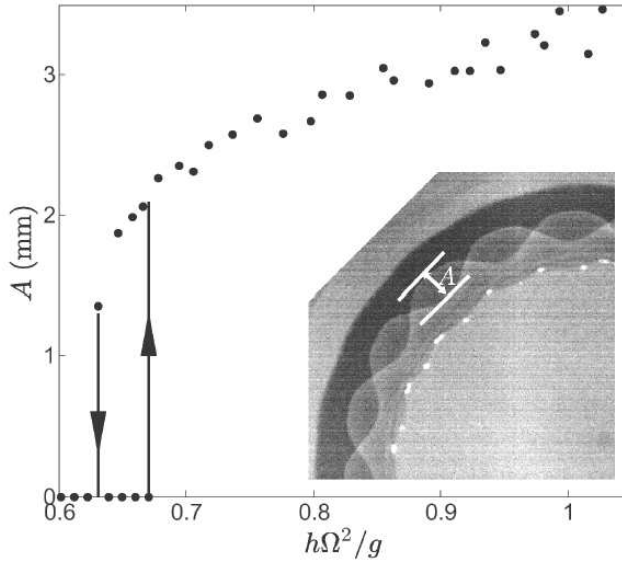


FIG. 4: Lateral amplitude of oscillation vs. non-dimensional acceleration ($h\Omega^2/g$) at $\Omega/2\pi = 30$ Hz. A is the transverse amplitude as indicated in the inset. This response curve shows hysteresis over driving acceleration between 0.63 and 0.67 g .

boundary condition, we can assume solutions such as

$$\zeta(\theta, z; t) = \sum \zeta_{mk}(t) e^{i(m\theta + kz)} \quad (3)$$

$$\phi(r, \theta, z; t) = \sum \frac{d\zeta_{mk}(t)}{dt} \frac{I_m(kr)}{kI'_m(kr_0)} e^{i(m\theta + kz)}. \quad (4)$$

where k is the axial wavenumber ($= 2\pi/L$; L is the wavelength) and m is the azimuthal wavenumber (in the direction of θ). Here, we assume that a/g is small and neglect higher azimuthal modes ($|m| > 3$). Using the symmetry $\zeta_{m,k} = -\zeta_{-m,k}$, setting the unphysical volume

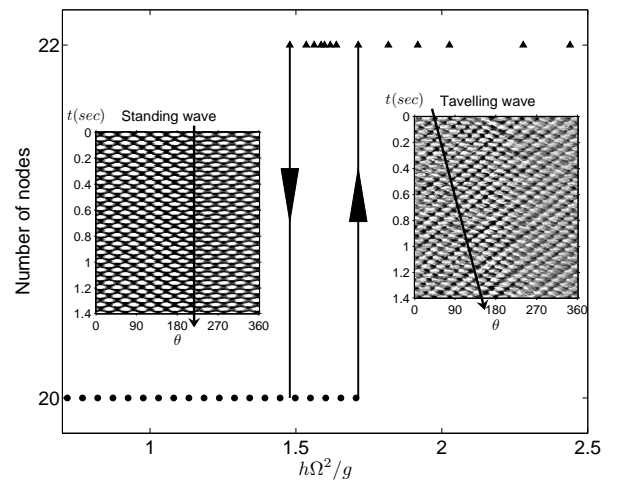


FIG. 5: Number of nodes vs. non-dimensional acceleration at $\Omega/2\pi = 30$ Hz. As the acceleration is slowly increased, the number of nodes changes from 20 to 22 when the acceleration is about $1.71 g$. When the acceleration decreases, the number of nodes returns back to 20 at $1.48 g$. The states shown in triangles (top branch) are associated with the travelling waves.

change term ζ_{0k} to be zero, and plugging Eqs. (3,4) into Eq. (1) yields

$$\begin{pmatrix} Z_{1k}\partial_{tt} + \sigma_{1k} & g_e(t) \\ g_e(t) & Z_{2k}\partial_{tt} + \sigma_{2k} \end{pmatrix} \begin{pmatrix} \zeta_{1k} \\ \zeta_{2k} \end{pmatrix} = 0, \quad (5)$$

where $Z_{mk} = I_m(kR)/kI'_m(kR)$ and $\sigma_{mk} = (\sigma/\rho) \cdot (k^2 + m^2/R^2 - 1/R^2)$. The surface deformation is assumed to be of the Floquet form ($\zeta_{mk} = e^{\tau t} \sum \zeta_n^{(m)} e^{in\Omega t}$) where $\tau = s + ia\Omega$ [4]. For subharmonic solutions ($\alpha = 1/2$), one gets the recursion relation:

$$H_n \zeta_n^{(m)} = \frac{a}{g} \left(\zeta_{n-1}^{(m)} + \zeta_{n+1}^{(m)} \right) + \mathcal{O}((a/g)^2), \quad (6)$$

where

$$H_n = [-1 + 4(Z_{1k}\omega_n^2 - \sigma_{1k})(Z_{2k}\omega_n^2 - \sigma_{2k})/g^2] \quad (7)$$

and $\omega_n = (1/2 + n)\Omega$. The problem of stability of the cylindrical fluid surface is reduced to finding the eigenvalues of Eq. (6) up to the order of a/g .

Figure 3 compares the observed patterns with theoretical predictions based on the model shown above. It is in good agreement with our experimental results observed close to the onset.

We also find experimentally that the onset of surface waves is hysteretic. Figure 4 shows the maximal displacement A between standing wave peaks over the course of an oscillation, as a function of dimensionless driving acceleration $h\Omega^2/g$, where h is the amplitude of plate oscillation. Crossing a critical amplitude from below

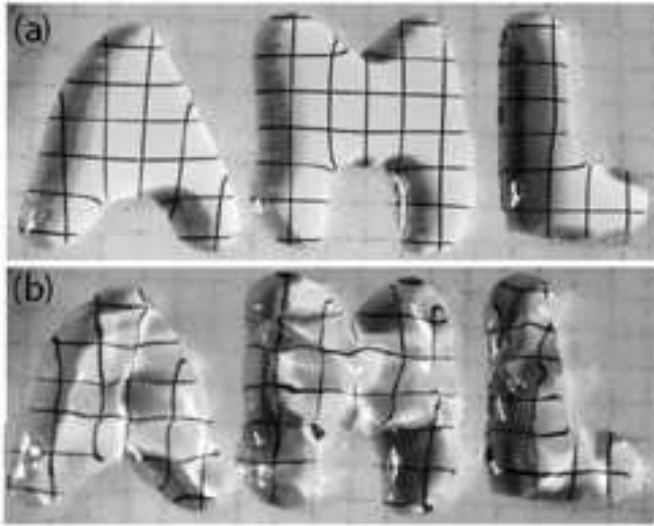


FIG. 6: (a) Below threshold, stable fluid surface constrained to three regions which are bordered by a hydrophobic coating. (b) Above the onset, unstable fluid surface vibrating at half of the driving frequency. At 50 Hz, fluid surfaces constrained to the shapes “A”, “M”, “L” become unstable at accelerations 2.51, 2.23 and 2.64 g , respectively.

shows the sharp transition to standing wave. This bifurcation is subcritical, and at intermediate accelerations ($0.63 g < h\Omega^2 < 0.67 g$) two stable states are observed.

Figure 5 shows yet another hysteretic transition in the number of surface nodes, at a higher dimensionless acceleration. Bistable surface waves with different numbers of nodes co-exist between $1.48 g$ and $1.71 g$. We find that the surface waves above this transition still oscillate at half the driving frequency, but now have more nodes and a finite drift speed (triangles). The inset images show the patterns of peaks (bright) and troughs (dark) in space-time. The arrows indicate the direction of azimuthal drift and its speed. If the acceleration is further increased to around $4 g$, the travelling surface waves become more spatially localized, and droplets are ejected.

Our masking technique can be used effectively to make complicated hydrophilic regions, and to investigate the dynamics of fluid volumes trapped within them. Figure 6 shows three separate fluid volumes bound within domains (the letter shapes A, M and L) of different shapes at both stable and unstable states. At fixed volume to base-area ratio of $0.16 \text{ cm}^3/\text{cm}^2$, which gives a fixed height for all shapes slightly above 0.18 cm , instability occurs at different thresholds for the different base shapes. The shape that with high aspect ratio (e.g. letter “L”) appears to have the highest threshold to instability. The top image shows these volumes at rest, where the transparent glass surface of the hydrophilic region reveals a square grid beneath. The bottom image shows the surface wave dynamics of these fluid volumes as revealed, at least in part, by the distortions of the underlying grid lines.

In this paper, we have studied the nature of surface waves on a semi-toroidal water volume that is being oscillated along its axis. The fluid volume is constrained to a precise geometric area (an annulus) by the patterning of the supporting surface into hydrophobic and hydrophilic regions. We find a hysteretic onset of azimuthal standing waves, and describe the observed dispersion relation by a simple linear model. For large forcing, we observe a transition, again hysteretic, to travelling waves with an increased number of nodes.

Authors thank A. Libchaber and V. Rom-Kedar for helpful discussions. This work is supported by DOE Grant DE-FG02-88ER25053.

- [1] M. Faraday, Phil. Trans. R. Soc. London **121**, 299 (1831).
- [2] T. B. Benjamin and F. Ursell, Proc. R. Soc. London A **225**, 505 (1954).
- [3] J. Miles and D. Henderson, Annu. Rev. Fluid Mech. **22**, 143 (1990).
- [4] K. Kumar, Proc. R. Soc. London A **452**, 1113 (1996).
- [5] E. A. Cerdá and E. L. Tirapegui, J. Fluid Mech. **368**, 195 (1998).
- [6] P. Chen and J. Viñals, Phys. Rev. E **60**, 559 (1999).
- [7] W. S. Edwards and S. Fauve, Phys. Rev. E **47**, R788 (1993).
- [8] L. Daudet, V. Ego, S. Manneville, and J. Bechhoefer, Europhys. Lett. **32**, 313 (1995).
- [9] H. W. Müller, Phys. Rev. Lett. **71**, 3287 (1993).
- [10] S. Ciliberto, S. Douady, and S. Fauve, Europhys. Lett. **15**, 23 (1991).
- [11] R. J. Lang, J. Acoust. Soc. Am. **34**, 6 (1962).
- [12] W. S. Edwards and S. Fauve, J. Fluid Mech. **278**, 123 (1994).
- [13] K. Kumar and K. M. S. Bajaj, Phys. Rev. E **52**, R4606 (1995).
- [14] A. Kudrolli and J. P. Gollub, Physica D **97**, 133 (1996).
- [15] R. Keolian, L. A. Turkevich, S. J. Puttermann, and I. Rudnick, Phys. Rev. Lett. **47**, 1133 (1981).
- [16] S. Douady, J. Fluid Mech. **221**, 383 (1990).
- [17] J. M. Vega, E. Knobloch, and C. Martel, Physica D **154**, 313 (2001).
- [18] F. J. Mancebo and J. M. Vega, J. Fluid Mech. **467**, 307 (2002).
- [19] T. B. Benjamin and J. C. Scott, J. Fluid Mech. **92**, 241 (1979).
- [20] C. Martel, J. A. Nicolás, and J. M. Vega, J. Fluid Mech. **360**, 213 (1998).
- [21] M.-T. Westra, D. J. Binks, and W. van de Water, J. Fluid Mech. **496**, 1 (2003).
- [22] H. Lamb, *Hydrodynamics* (Cambridge University Press, 1932).
- [23] X. Noblin, A. Buguin, and F. Brochard-Wyart, Eur. Phys. J. E **14**, 395 (2004).
- [24] A. Frohn and N. Roth, *Dynamics of Droplets* (Springer Press, 2000).
- [25] A. J. James, B. Vukasinovic, M. K. Smith, and A. Glezer, J. Fluid Mech. **476**, 1 (2003).
- [26] A. J. James, M. K. Smith, and A. Glezer, J. Fluid Mech. **476**, 29 (2003).